Mechanical Systems and Signal Processing 104 (2018) 19–35

Contents lists available at ScienceDirect

Mechanical Systems and Signal Processing

journal homepage: www.elsevier.com/locate/ymssp

Investigations on flexural wave propagation and attenuation in a modified one-dimensional acoustic black hole using a laser excitation technique

Hongli Ji [a,b], Jing Luo [a], Jinhao Qiu [a,*], Li Cheng [b,*]

[a] State Key Laboratory of Mechanics and Control of Mechanical Structures, Nanjing University of Aeronautics & Astronautics, Nanjing, China
[b] Department of Mechanical Engineering, Hong Kong Polytechnic University, Hung Hom, Kowloon, Hong Kong

ARTICLE INFO

Article history:
Received 2 June 2017
Received in revised form 21 October 2017
Accepted 24 October 2017

Keywords:
Acoustic black holes
Energy trapping
Reflection coefficient
Laser excitation technique
Damping layer

ABSTRACT

Acoustic Black Holes (ABHs), as a new type of passive structure for vibration damping enhancement and noise attenuation, have been drawing increasing attentions of many researchers. Due to the difficulty in manufacturing the sharp edges required by the ABH structures, it is important to understand the wave propagation and attenuation process in the presence of damping layers in non-ideal ABHs with a truncated edge. In this paper, an analytical expression of the wave reflection coefficient in a modified one-dimensional ABH is derived and a time-domain experimental method based on a laser excitation technique is used to visualize the wave propagation. In the experimental studies, the flexural waves in the ABH were excited by a scanning pulse laser and measured by a Laser Doppler Vibrometer (LDV). The incident wave and reflected wave were separated from the measured original wave field and the decrease of the wave velocity in the ABH was exhibited. The reflection coefficient was calculated from the ratio of the amplitude of the reflected wave to that of the incident wave for different ABH parameters and different thicknesses of the damping layer. The measured reflection coefficients were used to identify the unknown coefficients in the theoretical formula. The results confirm that there exists an optimal thickness for the damping layer, which leads to the minimum wave reflection. Based on the laser-induced visualization technique and various signal processing and feature extraction methods, the entire process of the wave propagation in a non-ideal one-dimensional ABH structure can be visualized and scrutinized.

1. Introduction

Recently, acoustic black holes (ABHs), as a new type of passive structure for vibration damping enhancement and noise attenuation, have drawn the attention of many researchers. The concept of the ABH was initially proposed by Mironov and Krylov in one-dimensional plates containing a power-law-profiled wedge, towards which the propagating flexural waves are slowed down [1–3]. When the power-law thickness profile, $h(x)$, satisfies

$$h(x) = \varepsilon x^m \quad (m \geqslant 2), \tag{1}$$

* Corresponding authors.
E-mail addresses: qiu@nuaa.edu.cn (J. Qiu), li.cheng@polyu.edu.cn (L. Cheng).

https://doi.org/10.1016/j.ymssp.2017.10.036
0888-3270/

in which x is the distance from the edge, ε is a constant scale factor, and m is a rational number, the flexural wave cannot reach the sharp edge and be reflected back in the ideal zero-thickness scenario. This leads to a drastic wave compression and energy trapping within the tapered wedge area. This phenomenon has been exploited to achieve efficient damping for flexural waves in plate-like structures using both one-dimensional and two-dimensional ABHs with a very small amount of damping materials covering the sharp edges [4]. The benefit of the wave manipulation through ABH effect is obvious. In terms of the energy utilization, the strong energy concentration facilitates and enhances the efficiency of the energy harvesting [5,6]. In terms of vibration and noise suppressions, it would be more advantageous and efficient to apply energy dissipation means such as coated damping layers only to the specific energy concentration areas, which is especially important in light-weighted structures used in aeronautical and automotive applications [7–11].

However, an ideal ABH structure is difficult to be realized due to the existing machining capability. Even in the ABH structures of composites, which are usually manufactured by layering up prepreg, ideal profiles are still difficult to be realized due to the thickness of prepreg. On the other hand, ideal ABHs are not suitable for real-world structures due to their intrinsic weakness in structural integrity and strength. Fabricated real-life wedges are always truncated to a certain residual thickness, which adversely affects their performance as 'black holes'. Without additional damping treatment, the typical values of the reflection coefficient in such materials as steel can become as large as 50–70%, which makes it impossible to use such wedges as practical vibration dampers. Although the situation can be improved by covering the wedge surfaces near the edges by thin absorbing layers [12–16], methods, be it theoretical or experimental, allowing for systematic analyses and the time-domain wave visualization are still very much limited.

Among existing theoretical and numerical studies, the geometrical acoustic approach was first proposed to analyze the flexural wave propagation in tailored wedges and to calculate the reflection coefficients under the hypothesis that the influence of the stiffness and the mass of the damping layer on the local dynamics of the ABH is negligible [17]. Under the umbrella of the geometrical acoustics, the reflection coefficient was analytically expressed as simplified formulae to taking into account the effect of a thin absorbing film for different power-law profiles of order m=2, 3, 4 and for a sinusoidal profile [12–14]. A different approach which is not limited by the hypotheses of the geometrical acoustics has been proposed by Georgiev et al. for beam structures using an impedance method [18], which in turn leads to a Riccati equation. This approach can only deal with a semi-infinite structure with the ABH on the edge, which is obviously different from the practical structures with finite size and real boundaries. On the other hand, most existing approaches consider the effect of a thin damping layer through Ross-Unar-Kerwin (RUK) model [19], which assumes the thickness of the damping layer is much smaller than that of the wedge. In practice, however, the thickness of even an extremely thin damping layer would be comparable to that of the wedge tip, where ABH effect is the largest, which suggests the importance of considering more practical cases. Besides, the optimal damping layer thickness depend on many factors, such as the tip thickness, the location, and the size [12–16]. In this regard, Tang et al. [20] show that the full coupling between the damping layers and the ABH taper can be taken into account using a semi-analytical model based on a Euler-Bernoulli beam. By using Mexican hat wavelet functions to approximate the flexural displacement, the governing equations are obtained using Lagrange's equations. The proposed model provides an efficient way to study the ABH feature and the effect of damping layers using a more realistic ABH-featured beam. However, in almost all the above works, frequency-domain approaches were used.

In addition to the theoretical studies, experimental investigations on ABH have also been conducted using a variety of beam-like and plate-like structures [4,9,11,15,21–23]. Bowyer investigated the effects of the different manufacturing processes and the tolerances on the vibration damping in structures with power-law-profiled edges [24]. Two-dimensional structures like rectangular plates, elliptical plates and circular plate with tapered indentations (pits) of power-law profile machined on the plates were also experimentally investigated [7,8–13]. Until now, with nearly no exception, all the experimental investigations on ABHs are carried out in the frequency domain, based on metrics such as frequency response function or point mobility. These experimental studies have confirmed the high efficiency of ABH for vibration damping enhancement. Although the ABH effect on the steady vibration response can be illustrated, the wave propagation process, which is very important for understanding the energy trapping process as well as the influence of various geometrical and structural imperfections of the structure, cannot be revealed. Despite the popular use of frequency-domain methods in engineering applications, time-domain methods are more attractive and insightful in revealing time-varying phenomena. Besides, as a more direct indicator of the ABH phenomenon, the reflection coefficient can provide invaluable information on the design of practical ABH structures, if it can be directly measured experimentally. One of the possible ways is the use of laser-based wave generation technology [25–28]. Yan investigated the effect of ABH structure on Lamb modes using laser-generated Lamb waves [27]. Huang also researched the wave energy focalization in a modified ABH structure using laser excitation technique [28]. The time-domain technique using laser excitation not only helps to understand the energy trapping effect of ABH qualitatively, but also provides a quantitative means to evaluate the ABH effect and to study the influence of parameters. A Kundt-like method was proposed by Denis for measurement of the reflection coefficient of a beam termination, but it cannot be used to show the wave propagation process of the ABH effect [29].

In order to achieve better understanding of the ABH effect and the calculation of the reflection coefficient directly, a time-domain experimental method is proposed to study some fundamental issues, including wave velocity decrease, wave package compression, edge reflection and attenuation along the propagation path. In the proposed method, the flexural wave in the ABH is generated by a scanning pulse laser and measured by Laser Doppler Vibrometer (LDV). Signal processing on the measured time-domain is then carried out for wave separations. Based on the laser-induced visualization technique and various signal processing and feature extraction methods [30], the entire process of the wave propagation in a non-ideal

one-dimensional ABH structure can be visualized and scrutinized. Owing to the unique feature of the proposed methodology, investigations of some key aspects in the ABH realizations, such as structural interaction between the damping layers, tip thickness of the ABH and the host structure, become possible. For example, it is shown that there exists an optimal thickness for the damping layer, to strike a balance between the energy focalization due to the ABH effect and the energy dissipation [12,16]. The excessive use of the damping layer may compromise or even jeopardize the ABH-induced energy focalization due to its dynamic interference with the host structure, leading to a reduced energy dissipation by the same token. In addition, the spatial evolution of the wave reflection coefficient can also be displayed, which could provide invaluable guidance to the design of practical ABH structures. The paper is organized as follows. An analytical expression of the reflection coefficient of wave in a modified one-dimensional ABH structure is derived in Section 2. The experimental system is then described and the measurement method is introduced. In Section 3, experimental results are presented to show the characteristics of one-dimensional ABH effect and evaluate the influences of various parameters on the reflection coefficient. Finally, conclusions are drawn in Section 4.

2. Analysis of decay and reflection of flexural wave in ABH

2.1. Wave equation and its solutions based on geometrical acoustics

Flexural waves in a one-dimensional ABH structure satisfy the following governing equation [2]:

$$\frac{\partial^2}{\partial x^2}\left(D(x)\frac{\partial^2 w}{\partial x^2}\right) - \omega^2 \rho h(x) w = 0 \tag{2}$$

where w is the transverse deflection of the structure, ρ is the density, $D(x) = Eh^3(x)/12(1-v^2)$ is the bending stiffness, and v and E are Poisson's ratio and Young's modulus, respectively. Based on the geometrical acoustic approximation, $w(x)$ can be expressed as [1,2,13]:

$$w(x) = A(x)e^{i\Phi(x)} \tag{3}$$

where $A(x)$ and $\Phi(x)$ are the amplitude and accumulated phase, respectively, $k_p = \omega/c_p$ and $c_p = 2c_t(1 - c_t^2/c_l^2)^{1/2}$ are, respectively, the wave number and the velocity of quasi-longitudinal wave in the plate, c_l and c_t are the phase velocities of the longitudinal and shear waves, respectively. The wave number can be expressed as [14]:

$$k(x) = 12^{1/4} k_p^{1/2} h^{-1/2}(x). \tag{4}$$

Since the increment of the phase angle in an infinitesimal distance dx is $k(x)dx$, the accumulated phase angle, $\Phi(x)$, from x_0 to x is expressed as

$$\Phi(x) = \int_{x_0}^{x} k(x)dx. \tag{5}$$

The above results are derived based on the assumption of the geometrical acoustic approximation that the variation of plate thickness is sufficiently smooth, *i.e.*

$$\frac{\boldsymbol{dk}}{\boldsymbol{dx}}\frac{1}{\boldsymbol{k}^2} \ll 1, \tag{6}$$

stipulating that, physically, the variation of the flexural wave number must be small over a distance of wavelength order.

If the thickness $h(x)$ satisfies Eq. (1) with $m \geqslant 2$ and $x_0 = 0$, then the accumulated phase angle Φ in Eq. (5) tends to infinity, indicating that the flexural wave will not reach the edge at $x = 0$ so that there is no reflection. That wedge, defined by Eq. (1) with $m \geqslant 2$, is referred to as the ideal one-dimensional ABH in the literature, also to be adopted in the present paper.

2.2. Reflections of the flexural waves at the truncated edge

Real-life fabricated wedges always contain truncated edges with a residual thickness. Albeit very small, it may adversely affect the acoustic black hole effect. For a wedge truncated at $x = x_0$, the lower integration limit x_0 in Eq. (5) is not zero and the accumulated phase angle will not be infinite. Therefore, as shown [1], wave reflections take place at the edge ($x = x_0$) and the attenuation of wave inside the ABH can only be due to the viscosity of the ABH material. The viscoelastic property of the ABH materials can be characterized by a complex modulus as:

$$E^* = E(1 + \mathrm{j}\eta) \tag{7}$$

where η is the loss factor of the material. In this case, the wave number is also complex. Because η is small, the terms in the complex wave number that contain the high orders of η can be neglected and the imaginary part can be expressed approximately in the following form [1,17]:

$$\mathrm{Im}\{k(x)\} = (\eta/4)\cdot 12^{1/4}k_p^{1/2}h^{-1/2}(x) \tag{8}$$

Since the attenuation of the flexural wave is induced by the viscosity property inside the ABH area, the reflection coefficient at an arbitrary position x can be expressed in the following form:

$$R_0 = \exp\left(-2\int_{x_0}^{x}\mathrm{Im}\{k(x)\}dx\right) \tag{9}$$

The reflection coefficient can be obtained by letting $x = x_B$ where x_B is the coordinate of the junction point between the uniform portion and the ABH portion of the structure, as shown in Fig. 1.

When covering the wedge surfaces near the edges with thin damping layers (see Fig. 1), e.g. by polymeric films, the simplest way of solving this problem is to use the available solutions obtained for surface-coated or sandwich plates. Using this approach [12,17], the imaginary part of a flexural wave number, Im $k(x)$, after taking into account both the effect of thin damping layers and that of the wedge material and the geometry, can be written as:

$$\mathrm{Im}k(x) = \left[\frac{12^{1/4}k_p^{1/2}}{h^{1/2}(x)}\right]\left[\frac{\eta}{4}+\frac{3}{2}\frac{\delta}{h(x)}\frac{E_2}{E_1}\mu\right] \tag{10}$$

where μ is the loss factor of the material of the absorbing layer, η is the loss factor of the wedge material. The additional flexural wave attenuation caused by the absorbing layer, as described by the second term in Eq. (10), is proportional to the ratio of the absorbing layer thickness δ to the plate thickness h, and to the ratio of Young's moduli, E_2/E_1, of the absorbing layer and the plate, respectively.

2.3. Reflection coefficient inside an ideal ABH

Based on Eq. (8), the integration in the exponent of Eq. (9) for an ideal ABH with quadratic shape, i.e. with $h(x) = \varepsilon x^2$, can be expressed in the following form:

$$\int_{x_0}^{x}\mathrm{Im}\{k(x)\}dx = \frac{12^{1/4}k_p^{1/2}\eta}{4\varepsilon^{1/2}}\ln\left(\frac{x}{x_0}\right) \tag{11}$$

Eq. (9) shows that the reflection coefficient, R_0, at a point x inside the ideal ABH can be expressed as:

$$R_0 = (x/x_0)^{-K}, \tag{12}$$

where

$$K = \frac{12^{1/4}k_p^{1/2}\eta}{2\varepsilon^{1/2}}. \tag{13}$$

Eq. (12) indicates that the reflection coefficient decreases according to an inverse power-law inside an ideal ABH.

If only one surface of the wedge is covered by a thin absorbing layer, the integration in the exponent of Eq. (9) becomes

$$\int_{x_0}^{x}\mathrm{Im}\{k(x)\}dx = \frac{12^{1/4}k_p^{1/2}\eta}{4\varepsilon^{1/2}}\ln\left(\frac{x}{x_0}\right)+\frac{3\times 12^{1/4}k_p^{1/2}\nu\delta}{8\varepsilon^{3/2}}\frac{E_2}{E_1}\frac{1}{x_0^2}\left(1-\frac{x_0^2}{x^2}\right) \tag{14}$$

Obviously, the substitution of Eq. (14) into Eq. (9) gives a more complex expression of R_0.

2.4. Reflection coefficient inside ABH partially covered with absorbing layers

As discussed previously, an ideal ABH structure is difficult to be realized and difficult to be used in practice. The former is due to the limited machining capability, thus resulting unavoidable alteration to ABH structures; while the latter being related to the structural weakness and deficiency resulting from the stringent thickness requirement of the ideal ABH profile.

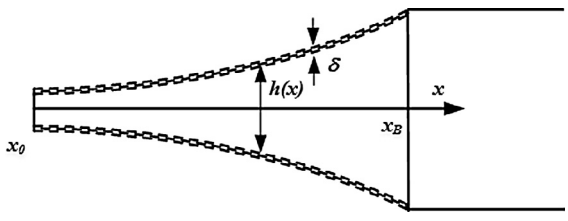

Fig. 1. Truncated wedge covered by thin absorbing layers.

For this reason, many new kinds of modified thickness profile have been proposed [28]. In the present work, an ABH wedge with one kind of modified thickness profile is considered. The modified profile is generally described by the following form:

$$h(x) = \varepsilon x^2 + h_0 \tag{15}$$

which has a non-zero thickness h_0 at x = 0. The integration in the exponent of Eq. (9) becomes:

$$\int_0^x \mathrm{Im}\{k(x)\}dx = \frac{12^{1/4}k_p^{1/2}\eta}{4\varepsilon^{1/2}} \ln\left(\sqrt{\frac{\varepsilon}{h_0}}x + \sqrt{\frac{\varepsilon x^2}{h_0}+1}\right) \tag{16}$$

The reflection coefficient at any given point x inside the modified ABH can be expressed as:

$$R_0(x) = \left(\sqrt{\frac{\varepsilon x^2}{h_0}} + \sqrt{\frac{\varepsilon x^2}{h_0}+1}\right)^{-K}. \tag{17}$$

The variation of R_0 is more complex in the modified ABH as compared with the conventional one.

With only one surface of the wedge covered, the integration term in the exponent of Eq. (9) becomes

$$\int_{x_0}^x \mathrm{Im}\{k(x)\}dx = \frac{12^{1/4}k_p^{1/2}\eta}{4\varepsilon^{1/2}} \ln\left(\sqrt{\frac{\varepsilon}{h_0}}x + \sqrt{\frac{\varepsilon x^2}{h_0}+1}\right) + \frac{3\times 12^{1/4}k_p^{1/2}\nu}{8\varepsilon^{1/2}} \frac{E_2\delta}{E_1 h_0} \frac{\sqrt{\varepsilon x^2/h_0}}{\sqrt{\varepsilon x^2/h_0+1}} \tag{18}$$

which results in

$$R_0(x) = \left(\sqrt{\frac{\varepsilon x^2}{h_0}} + \sqrt{\frac{\varepsilon x^2}{h_0}+1}\right)^{-K} \cdot \exp\left\{-K_2 \frac{\sqrt{\varepsilon x^2/h_0}}{\sqrt{\varepsilon x^2/h_0+1}}\right\}. \tag{19}$$

where

$$K_2 = \frac{3\times 12^{1/4}k_p^{1/2}\nu}{4\varepsilon^{1/2}} \frac{E_2\delta}{E_1 h_0}. \tag{20}$$

During the derivation of the above expressions of the reflection coefficient without and with damping layer, the reflection of the edge is considered to be perfect. The attenuation is induced only by the materials, ABH structure itself and the damping layer. Given an imperfect edge, its reflection characteristic can be symbolically represented by a coefficient $R_E < 1$. The reflection coefficient at any point x inside the modified ABH can then be expressed as

$$R(x) = R_E \cdot R_0(x). \tag{21}$$

If the modified ABH is partially covered with a damping layer in the area from $x = 0$ to $x = x_d$, Eq. (19) holds for $0 \leqslant x \leqslant x_d$. In the range of $x_d \leqslant x \leqslant L_{\mathrm{ABH}}$, where L_{ABH} is the length of ABH, Eq. (19) should be re-written as:

$$R_0(x) = \left(\sqrt{\frac{\varepsilon x^2}{h_0}} + \sqrt{\frac{\varepsilon x^2}{h_0}+1}\right)^{-K} \cdot \exp\left\{-K_2 \frac{\sqrt{\varepsilon x_d^2/h_0}}{\sqrt{\varepsilon x_d^2/h_0+1}}\right\}. \tag{22}$$

3. Experimental measurement of wave propagation

3.1. Tested plate with one-dimensional ABH

A rectangular steel plate incorporating a wedge with a modified one-dimensional thickness profile, as shown in Fig. 2, is considered. The length L_1, width L_3 and thickness h_2 of the plate are 350 mm, 240 mm and 6 mm, respectively. The one-dimensional ABH, of 100 mm long, is machined through a milling process in the length direction. The minimum thickness h_1 at the edge tip is 0.1mm. In the coordinate system defined in Fig. 2, the thickness profile of the plate, $h(x)$, is expressed in following form.

$$h(x) = \begin{cases} 0.006 & 0 < x \leqslant 0.06 \\ 0.59(x-0.16)^2 + 0.0001 & 0.06 < x \leqslant 0.16 \end{cases} \tag{23}$$

In which, ε is set to 0.59, and m to 2. The dimensions and material properties of the plate are given in Table 1.

To investigate the influence of the damping materials on the reflection coefficient of the ABH, a damping layer was bonded on the flat side of the taper in the range 0.145 m $< x \leqslant$ 0.16 m. The size of the damping layer is 0.015 m in the x direction and 0.24 m in the width direction of the plate (the same width as the plate). The thickness of the damping layer was varied and set to different values. The density of the damping layer is 318 kg/m^3 and its loss factor is 0.18.

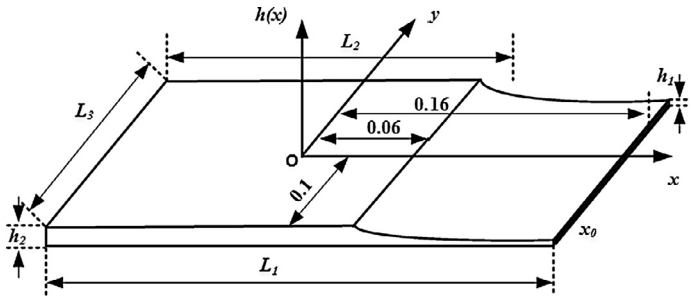

Fig. 2. The tested plate with a ABH profile.

Table 1
Material properties and dimensions of the plate and the damping layer.

The tested plate		
Dimensions	L_1	0.35 m
	L_2	0.25 m
	L_3	0.24 m
	h_1	0.0001 m
	h_2	0.006 m
Material properties	Young's modulus E	210 GPa
	Density ρ	7800 kg/m^3
	Poisson's ratio v	0.3
The damping layer		
Dimensions	Length	0.015 m
	Width	0.24 m
	Thickness	A variable (from 0.3 mm to 2 mm)
Material properties	Loss factor	0.18
	Density	318 kg/m^3

3.2. Experimental system for wave visualization

Different from the traditional frequency-domain methods, a time-domain technique based on a laser-acoustic system was used for the wave-field visualization and the identification of parameters such as the reflection coefficient. The time-domain method has advantages in describing the wave propagation process both qualitatively and quantitatively. The video visualization of the wave is one of the advantages of the time-domain technique in the qualitative aspect, which allows a better understanding of the wave propagation and trapping process, as opposed to the frequency-domain approaches which only give the end results. In the quantitative aspect, the variation of wave amplitude along the direction of propagation can be measured and the reflection coefficient as a function of the location can be calculated. This is particularly important for future applications where geometrical or manufacturing imperfections may occur and adversely affect the expected ABH effects. Ultrasonic wave visualization technique based on a laser ultrasonic system provides new paradigms, which have been extensively studied and widely used in various applications such as nondestructive evaluations (NDE) [30–33]. However, very few researches have been reported on applications of laser vibrometer on wave visualization in ABHs [25–28]. In this study, an in-house system based on laser vibrometer is used for visualization of bending waves and estimation of the reflection coefficient in an ABH structure. The system is similar to the one developed by the authors and used for Lamb waves in anisotropic composite structures [28], using AE sensors for response measurement. The experimental set-up, shown in Figs. 3 and 4, uses non-contacting excitation and sensing. Major components of the system include a pulse laser generator (YAG laser, Ultra-100, Quantel corp., USA), a vibrometer sensor head (OFV-505, Polytec, Canada), a vibrometer controller (OFV-5000, Polytec, Canada), a high-speed digitizer (PXI-5105, NI corp., USA) and an analog output module (cRIO-9263, NI corp., USA) (TSH8203H, Century Sunny corp., China).

The measurement area over the plate is meshed into a grid with a fixed distance in both x and y directions. The laser generator generates laser pulses with a repeating frequency of 20 Hz and a maximum energy of 55 mJ. When the pulse laser is irradiated at each grid point on the surface of the structure, it generates an impulse force and consequently excites the elastic waves due to the thermo-elastic effect. Synchronized with the excitation, the plate response is measured by the laser Doppler vibrometer at a fixed point on the structure. For the wave field visualization, the measurement process is repeated by exciting all the grid points in the predetermined two-dimensional measurement area as displayed in Fig. 5. Changes of the excitation point are achieved by rotating a two-dimensional mirror. On the basis of the reciprocal theorem in elastodynamics, the location of the excitation and the location of the measurement point can be exchanged in the spatial area. For a given time instant, the wave field at any specific moment can be displayed. Since the excitation force due to the laser irradiation is

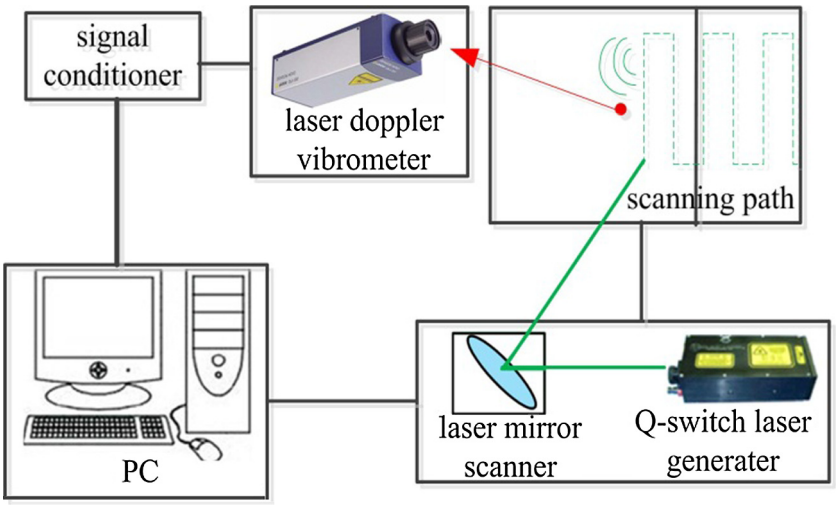

Fig. 3. Schematic diagram of the laser ultrasonic system.

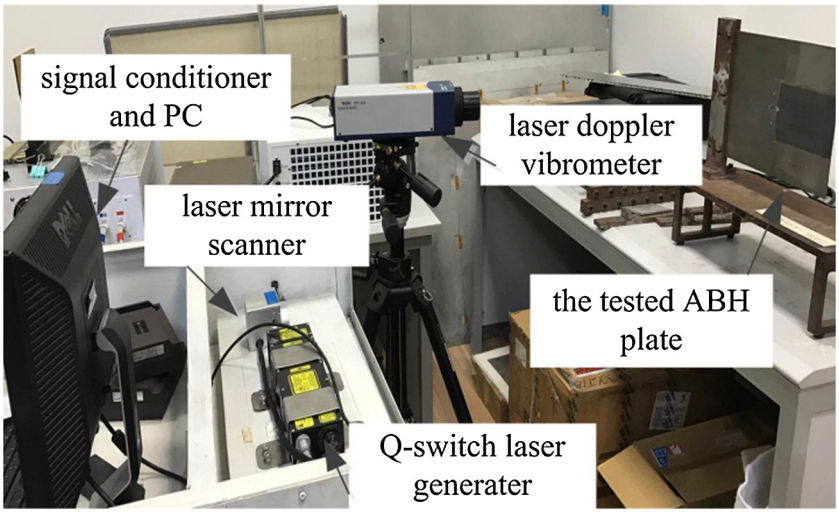

Fig. 4. Laser-ultrasonic system.

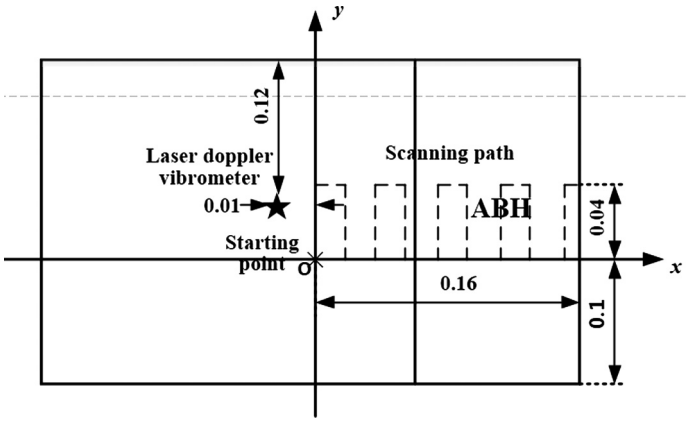

Fig. 5. The scanning path.

a wideband signal, wavelet analysis is used to extract the signal in a given frequency range of interest. The response at each scanning point can be plotted on an intensity snapshot map to represent the wave-field, successive display of which in a time series gives the wave propagation pattern. Using this experimental system, a series of tests are conducted in time domain.

3.3. Generation of wave field

The experiment was conducted using the experimental set-up shown in Fig. 4. The scanning area was 0.16×0.04 m with a spatial scanning interval of 0.001 m, giving a total of 6601 scanning points, as shown in Fig. 5. The starting point was the origin of the coordinate system, while the measurement point of the laser Doppler vibrometer was fixed at 0.01 m from the origin in the negative x direction and 0.02 m from the y axis. The LDV was used to collect the response signal with a frequency limit under 100 kHz. The sampling frequency was set to be 1×10^7 Hz to guarantee the precision of the wave-field visualization and the sampling time was set to 800 μs (8000 sampling point) for each excitation to ensure that the whole field of flexural wave propagation was recorded. The velocity signal measured by the laser Doppler vibrometer is denoted by $v(x_i, y_j, t_l)$, where (x_i, y_j), $(i = 1, \ldots, 161; j = 1, \ldots, 41)$ are the coordinates of the excitation points and t_l $(l = 1, \ldots, 8000)$ are the sampling time of the response. According to the reciprocal theorem of elastodynamics, $v(x_i, y_j, t_l)$ is equivalent to the discretization of the velocity field $v(x, y, t)$ when a pulse excitation is applied at the sensing point.

The wave visualization uses the measured velocity field, $v(x, y, t)$. Although it is different from the displacement field $w(x, y, t)$, they are considered to be proportional to each other for a given frequency. Hence all the results derived based on the displacement field are still valid for velocity field when the frequency is fixed. Because the response is measured only at one point, the obtained wave field $v(x, y, t)$ has a circular wave front. The objective of this paper is to investigate the wave propagation and attenuation process in non-ideal ABHs with a truncated edge in the presence of damping layers using a time-domain approach. Therefore, the way that the wave varies inside an ABH and how the damping layer influences the wave amplitude variation are the main focus of the paper. Hence, plane waves, the amplitude of which is independent of the propagation distance in an undamped uniform media, is preferred, as opposed to circular waves whose amplitude decreases with the propagation distance. To generate the wave pattern corresponding to the 1D plane wave incidence, a virtual sensor approach was used to convert the wave field. To this end, it is assumed that multiple virtual sensors exist at points $(-0.01, 0.02 + \lambda\Delta)$, where $\lambda = \pm 1, \ldots, \pm 10$ and $\Delta = 0.001$. The wave fields at the virtual sensor positions are then obtained by shifting the wave field $v(x, y, t)$ in the y direction, *i.e*, $v(x, y + j\Delta, t)$. A sketch showing the victual sensors is given in Fig. 6. The one-dimensional wave field can be obtained from the following equation:

$$\bar{v}(x, y, t) = \frac{1}{21} \sum_{\lambda=-10}^{10} v(x, y + \lambda\Delta, t) \tag{24}$$

The wave field $\bar{v}(x, y, t)$ is approximately one-dimensional in the region $0.01 \leqslant y \leqslant 0.03$. For convenience, $\bar{v}(x, y, t)$ will be written as $v(x, y, t)$ in the subsequent discussions. In the range $0.01 \leqslant y \leqslant 0.03$, the wave field $v(x, y, t)$ can be expressed

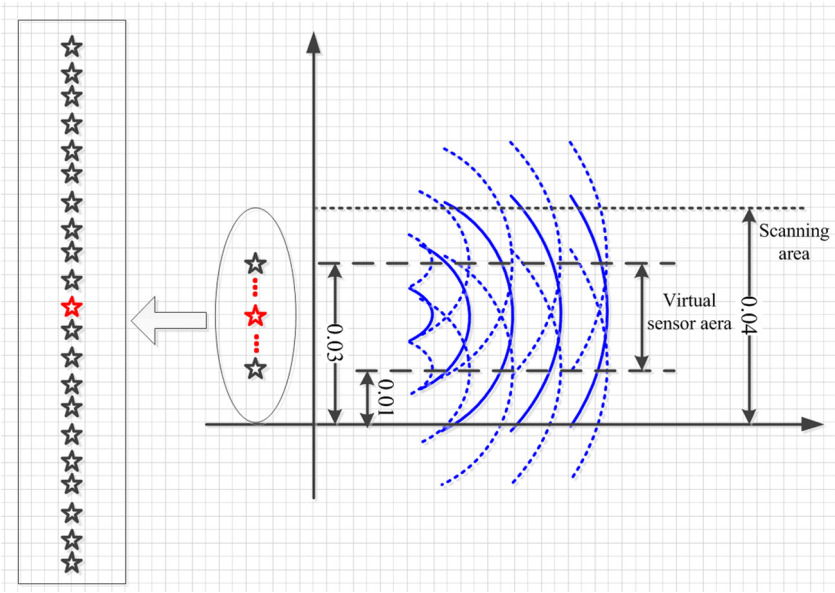

Fig. 6. Schematic diagram of virtual sensors.

as $v(x,t)$, independent of y. The wideband $v(x,t)$ is also converted to a single-frequency signal by using the wavelet method before further processing is conducted.

3.4. Wave separation and extraction of the reflection coefficient

The reflection coefficient is an important indicator to evaluate the wave reflection by the truncated edge of ABHs. In order to calculate the reflection coefficient, it is necessary to separate the incident wave and reflect wave from the measured wave field, $w(x, t)$, which can be converted to the one-dimensional wave field at each single-frequency using the wavelet method. Obviously, $w(x, t)$ contains both the incident wave and the reflected wave, expressed as:

$$w(x,t) = w_i(x,t) + w_r(x,t) \tag{24}$$

or

$$w(x,t) = A(\omega)\cos(\omega t - kx) + B(\omega)cos(\omega t + kx + \phi) \tag{25}$$

where $w_i(x,t)$ and $w_r(x,t)$ are incident and reflected wave, respectively, $\omega = 2\pi f$ is the angular frequency, ϕ is the phase shift between the incident and the reflected wave [30,31], the scalar coefficients A and B represent their respective magnitude.

The major difference between the incident and the reflected waves is the sign in front of the wavenumber k, negative for the wave propagating in the positive x direction and vise versa. The 2D-FT can be used to separate the waves with opposite propagation directions [34,35]. The spectrum in the wavenumber-frequency domain, $W(k,\omega)$, can be obtained by:

$$W(k,\omega) = \int_{-\infty}^{\infty}\int_{-\infty}^{\infty} w(x,t)\exp[-j(\omega t + kx)]dxdt \tag{26}$$

where j is the imaginary unit. In the (k,ω) domain, the region of $\omega > 0$ is meaningful in physics, while the area of $\omega < 0$ is the symmetrical component brought up by Fourier transformation, which cannot be ignored during inverse transformation because it is the symmetrical image of the positive ω components. As discussed above, the sign of wavenumber k determines the direction of wave propagation. Hence, the sign of the product $k\omega$ can be used to judge the direction of the wave propagation and to separate the incident wave from the reflected wave, which is crucial for the topic investigated in this paper. In the (k,ω) domain, the spectrum can be divided into four regions according to the sign of ω and k. Therefore, the region with $k\omega > 0$ represents the incident component, while region $k\omega < 0$ represents the reflected component. For the wave separation, two window functions, $F_i(k,\omega)$ and $F_r(k,\omega)$, are used as filters:

$$W_{i(r)}(k,\omega) = W(k,\omega)F_{i(r)}(k,\omega) \tag{27}$$

where $W_{i(r)}(k,\omega)$ denotes either the incident or the reflected wave in (k,ω) domain, with

$$F_{i(r)}(k,\omega) = \begin{cases} 1 & k\omega > 0\ (k\omega < 0) \\ 0 & \text{else} \end{cases} \tag{28}$$

The two-dimensional inverse Fourier transform (2D-IFT) is then applied to recover the time domain signals of these two components as follows:

$$w_{i(r)}(x,t) = \frac{1}{2\pi}\int_{-\infty}^{\infty}\int_{-\infty}^{\infty} W_{i(r)}(k,\omega) * \exp[j(\omega t + kx)]d\omega dk \tag{29}$$

This allows the calculation of the refection coefficient, defined as:

$$R_0(\omega) = B(\omega)/A(\omega). \tag{30}$$

Since the wave-field is defined at discrete points, both in time and space, the above Fourier transform can be realized by fast Fourier transform (FFT).

4. Results and discussions

4.1. Visualization of the wave field and energy distribution

As introduced above, when the flexural waves propagate along a one-dimensional ABH structure, their vibration amplitude will increase while the phase velocity will decrease gradually, generating energy focalization. In this section, these features will be investigated in time domain using experimental data to show the influence of the ABH effect on wave propagation process and to verify the feasibility of the proposed experimental method.

According to many past studies, the effective frequency range of ABH effects actually depends on the structural size as well as that of the ABH taper. When linear vibration theory holds, simple scaling laws exist which allow the prediction of the wave propagation and vibrational characteristics of a structure when its geometric dimension is scaled by a certain scaling ratio. Therefore, we would expect the effective frequency range of the ABH effects to be reduced if the structural size (along with the ABH taper size) is large enough, to eventually approach the application range for automotive and aero appli-

cations. Other means to ensure low-frequency ABH effects have also been proposed in the literature [36,37]. However, this issue needs a more systematic analysis and quantification before conclusions can be drawn. Since the objective of the present work is to examine the wave propagation and focalization based on an experimental technique, and it was difficult to experimentally test a structure of large size, we prefer not to include this low-frequency issue in the present paper.

Bending waves are dispersive in nature and the relationship between the wavenumber k and frequency in a wide range of frequencies can be used to characterize the wave dispersion characteristics. Since the fundamental mechanism of the energy trapping is the same for any frequencies above the cut-on. In the present work, signals extracted from the original wave field at specific frequency are used. The reasons to filter the broadband signals are twofold. The first reason is linked to the need of calculating the reflection coefficient at a specific frequency due to its frequency dependent nature. Second, bending waves are inherently dispersive, that is, waves of different frequencies travel at different group velocities. Hence, it is impossible to calculate the attenuation of wave amplitude if the signal is wideband. As a representative example, 30 kHz is selected for the visualization of the wave field and energy distribution. The reason for choosing 30 kHz is that, at this frequency, the signal-to-noise ratio is relatively high so that better results can be obtained. Signals extracted from the original wave field at 30 kHz, with the wave field at $t = 0.14$ ms shown in Fig. 7 are used. The time $t = 0.14$ ms is chosen to avoid the wave reflection from the boundary within this time. It can be seen that the vibrational amplitude in the sharp edge is indeed much larger than that in the flat region and the wavelength of flexural wave becomes shorter and shorter as it approaches the edge. This demonstrates the energy concentration near the sharp edge as predicted by the theory. The whole process of wave propagation and energy concentration can be better visualized in the form of a movie by arranging wave field of time instance in a chronological order.

To better quantify the phenomenon, the corresponding displacement signal along the line $y = 0.02$ m at $t = 0.14$ ms is extracted from the result in Fig. 7 and is explicitly shown in Fig. 8. It is obvious that when the flexural wave propagates in the ABH region toward the sharp edge, both the wave amplitude and the wave number increase, consistent with the expected ABH effect.

4.2. Decrease of the wave velocity in the ABH area

Because $c = \omega/k$, using the wavenumber in Eq. (4) the phase velocity can be written as:

$$c_p = \sqrt{2\pi f h}\left[\frac{E}{12\rho(1-v^2)}\right]^{1/4} \tag{31}$$

Substitution of Eq. (23) into Eq. (31) gives the theoretical relationship between the phase velocity c_p and the location x**.** In the flat region of $0 < x \leqslant 0.06$ m, the phase velocity is constant, while in the ABH area with $0.06 < x \leqslant 0.16$ m, the theoretical phase velocity varies as a function of position x:

$$c_p = \sqrt{\frac{\pi}{\sqrt{3}} f[0.56\cdot(x-0.16)^2 + 0.0001]}\left[\frac{E}{\rho(1-v^2)}\right]^{1/4}. \tag{32}$$

Obviously, the phase velocity depends also on the frequency of the wave.

The theoretically predicted phase velocity and the experimentally measured one are compared. The signal $w(x,t)$ at $y = 0.02$ m is plotted in Fig. 10 with time t as the horizontal axis and position x as the vertical axis. Defined as the derivative of the distance x with respect to time t, the phase velocity equals to the slope of the fringes, which have the same phase. As shown in Fig. 9, one of the fringes was selected for calculation of phase velocity.

Using the geometrical and material parameters of the test sample in Eq. (32) yields the theoretical velocities at different positions, which are plotted in Fig. 10 together with the experimental results. The material parameters used in the calculation are calibrated using the data obtained in the uniform region of the plate. As shown in Fig. 10, the theoretically calculated and the experimentally measured velocities in the ABH region are in good agreement, with an error typically less than 5%. The phase velocity indeed decreases as the wave packet propagates toward the sharp edge, in a quasi-linear manner.

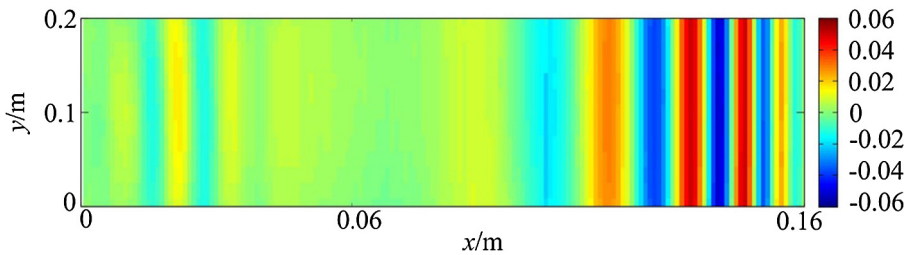

Fig. 7. Wave field of 30 kHz at t = 0.14 ms.

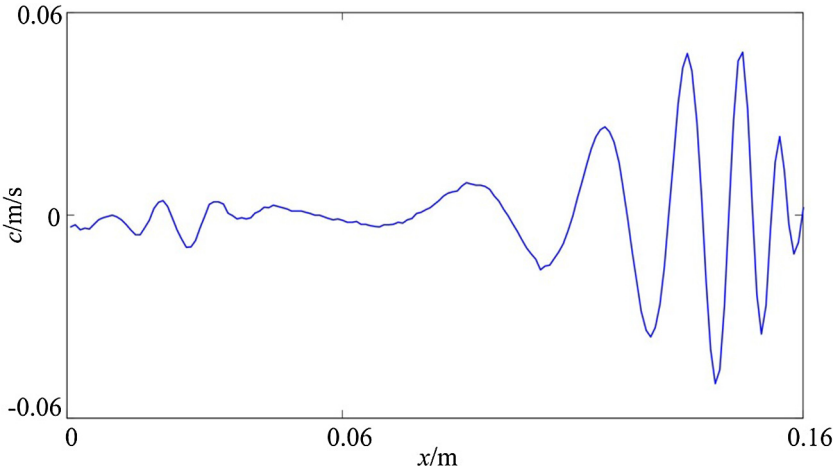

Fig. 8. Relationship of vibrational amplitude and distance x.

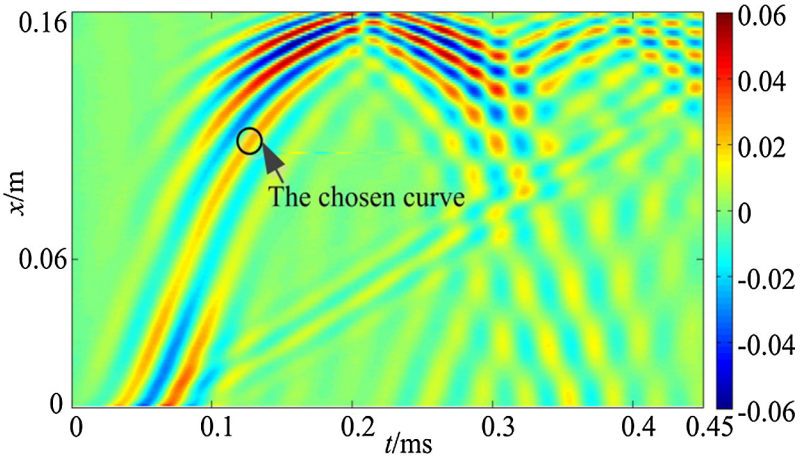

Fig. 9. Signal $v(x,t)$ at $y = 0.02$ m and $f = 30$ kHz plotted in the distance x – time t plane.

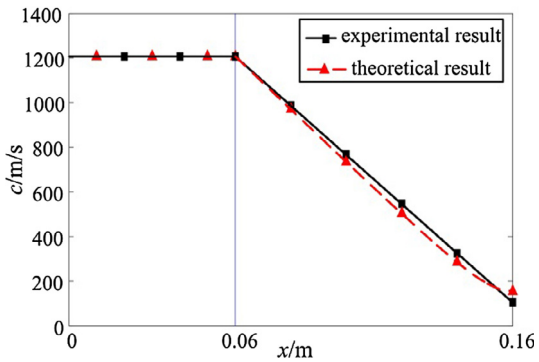

Fig. 10. Phase velocity c_p as a function of position x.

4.3. Reflection of the wave by the edge

To exact the reflection coefficient, the signal $v(x,y,t)$ along the line $y = 0.02$ m is used again, at the same frequency of 30 kHz. Using the same set of data (shown in Fig. 9), the incident and the reflected waves are separated from $v(x,t)$ using the method detailed in Section 3.4 and the results are shown in Fig. 11.

Since the amplitudes of the incident wave and the reflected wave vary with the coordinate x, it is necessary to select a suitable value of x to define the reflection coefficient. In the present case, two representative positions are chosen. The first one is the junction between the uniform portion and the ABH portion, at $x = 0.06$ m. This position is important to evaluate the wave attenuation induced by the whole ABH. The second point is located at $x = 0.145$ m, corresponding to the boundary between the ABH regions without and with the damping layer, to be considered in the next section.

The time traces of the velocities of the original, incident and reflected waves at $x = 0.06$ m and $x = 0.145$ m are extracted from Figs. 9 and 11, and the results are shown in Figs. 12 and 13, respectively. Obviously, waves propagate in the form of a wave packet, as a result of the pulse force excitation. Hence the maximum magnitude of the envelope of incident wave and that of the reflected wave are defined as the amplitudes A and B, respectively, which can be obtained by using wavelet analysis of the signals as shown in Figs. 12 and 13. After A and B are obtained, the reflection coefficient $R_0 = B/A$ can be calculated. Calculated R_0 is 0.5338 at $x = 0.06$m and 0.8934 at $x = 0.145$ m, respectively. The difference in the two R_0 values indicates that a significant portion of the incident wave is reflected from the edge and part of the reflected energy is dissipated during the propagation process inside the ABH. The result also confirms the fact that even a very small residual thickness at the sharp edge has a significant impact on the reflection coefficient, destroying the zero-reflection character of ideal one-dimensional ABH structure [3,12].

As shown in Section 3.4, the amplitude of the incident wave A and that of the reflected wave B are frequency dependent due to the dispersive characteristics of the flexural waves. Therefore, the reflection coefficient is, in principle, also frequency dependent. Fig. 14 shows the experimental result of the reflection coefficient versus frequency at $x = 0.145$ m. The result indicates that the frequency has only minor influence on the reflection coefficient.

4.4. Influence of the damping layer

Since even a small residual thickness at the sharp edge of an ABH can yield significant wave reflection [12–16], it is of great importance to investigate the influence of the damping layer bonded on the surface of the ABH taper. On the other hand, it is obvious that in a non-ideal ABH configuration, the wave energy is dissipated during the wave propagation process. Hence the relationship between the reflection coefficient and its position inside the ABH needs to be investigated, to be compared with the theoretical formulae derived in the Section 2.4. The configuration used is the one with a damping strip bonded on the flat surface of the test sample in the range $0.145 < x \leqslant 0.16$, as shown in Fig. 2.

Obtained from the same experimental procedure and data processing, Fig. 15(a) and (b) show the incident wave $v_i(x,t)$ and the reflected wave $v_r(x,t)$ at $f = 30$ kHz and $y = 0.02$ m when the bonded damping layer is 0.5 mm thick. Compared with Fig. 11(b), it can be seen that the reflected wave in Fig. 15(b) is now much smaller, as a result of the increased energy dissipation. The time response at $x = 0.06$ m and $x = 0.145$ m are obtained from the wave field and plotted in Figs. 16 and 17, respectively. Extracted from the magnitudes of the incident and reflected wave packets, the reflection coefficient R_0 are 0.3724 and 0.5556, respectively for the two positions, both being smaller than their corresponding counterparts without a damping strip. The result confirms the fact that the thin absorbing strip located near the sharp edge can significantly reduce the reflection coefficient [3,12], which also prove that the laser excitation technique is valid.

The reflection coefficient is expected to depend on both the thickness of the damping layer and the position [3,12]. In order to investigate this, the reflection coefficient at different location in x direction is measured using the above method when damping layers of different thickness are bonded on the surface. Five cases, including the one without damping layer and four other cases with four different damping layers, of 0.3 mm, 0.5 mm, 1 mm and 2 mm in thickness, are considered.

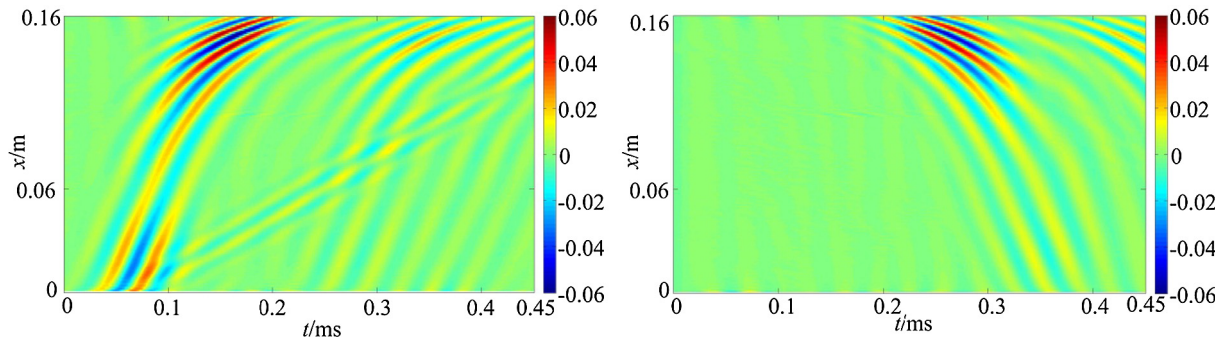

Fig. 11. Wave field in space-time domain $(x,\ t)$ at 30 kHz: (a) incident wave; (b) reflected wave.

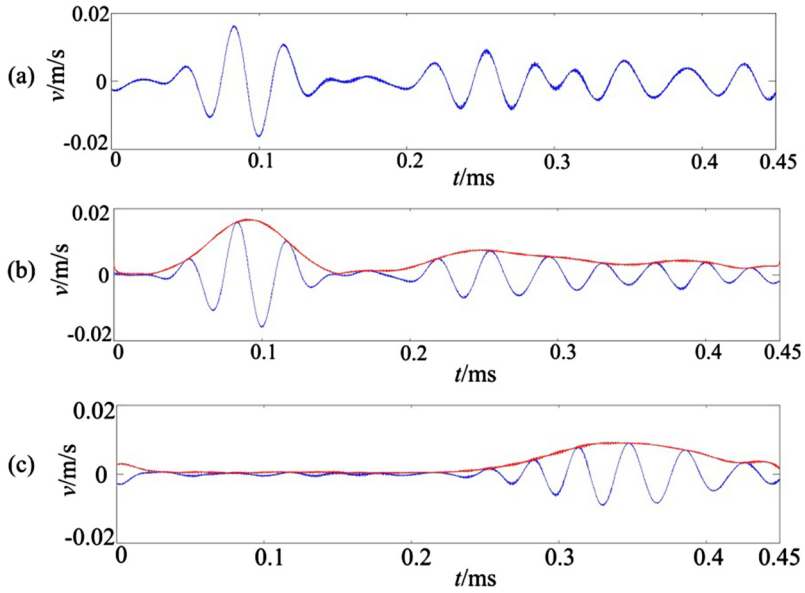

Fig. 12. Signal of 30 kHz at $x = 0.06$ m: (a) original wave; (b) incident wave; (c) reflected wave.

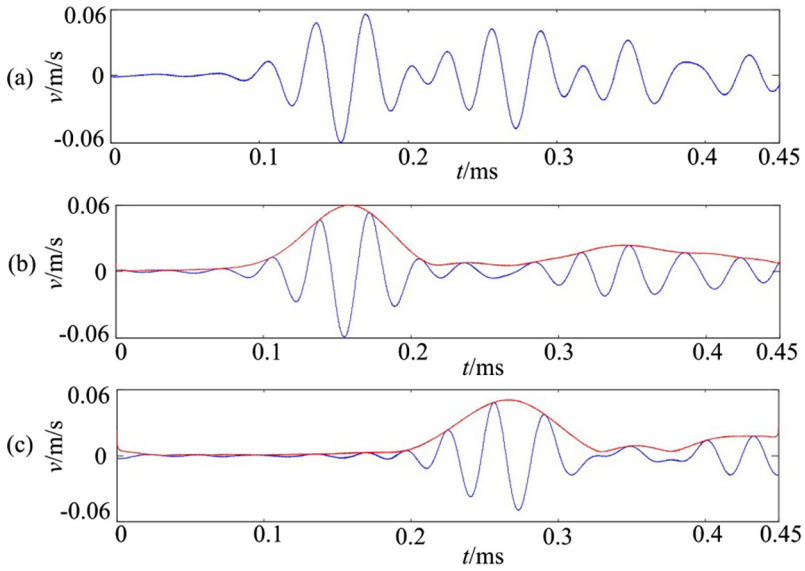

Fig. 13. Signal of 30 kHz at $x = 0.145$ m: (a) original wave; (b) incident wave; (c) reflected wave.

The data of reflection coefficient measured in the case without damping layer is used to fit the curve of Eq. (17) by identifying the unknown constant K_1 based on the LMS method, which minimizes the least meaning square value of the error. The data of the other four cases are then used to fit the curve of Eq. (19) by identifying the unknown constant K_2 using the same method. The obtained curves and the experimental data of all five cases are plotted in Fig. 18. The reflection coefficient R_E at the edge and the reflection coefficient R_0 at $x = 0.06$ m and $x = 0.145$ m are plotted in Fig. 19.

Although the measured data of the reflection coefficient are quite dispersive, the fitted curves give reasonable consistent results, as shown in Fig. 18. It is obvious that the reflection coefficient decreases as the distance from the sharp edge (at x = 0.16 m) increases due to the wave attenuation in the propagation process. When a damping strip is bonded near the sharp edge from $x = 0.145$ m to $x = 0.16$ m, a stronger wave attenuation is induced because of the high viscosity of the damping material. The influence of the thickness of the damping layer on the reflection coefficient at $x = 0.06$ m, $x = 0.145$ m and $x = 0.16$ m is shown in Fig. 19. Obviously, the reflection at the edge $x = 0.16$ m is not perfect, being not exactly equal to, but smaller than 1 (R_E defined in Eq. (21). It is also influenced by the thickness of the damping. The reflection coefficient

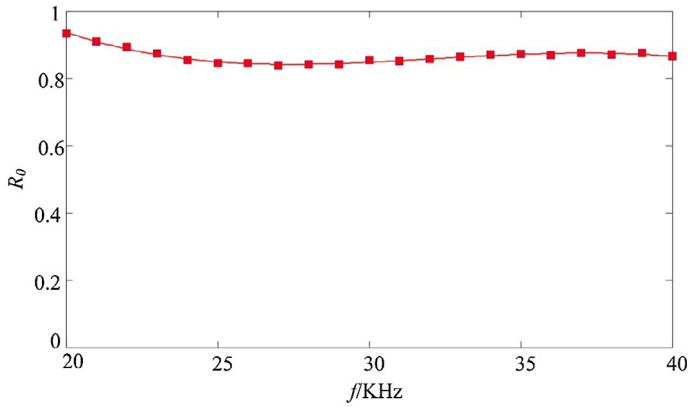

Fig. 14. Relationship of reflection coefficient and frequency at $x = 0.145$ m.

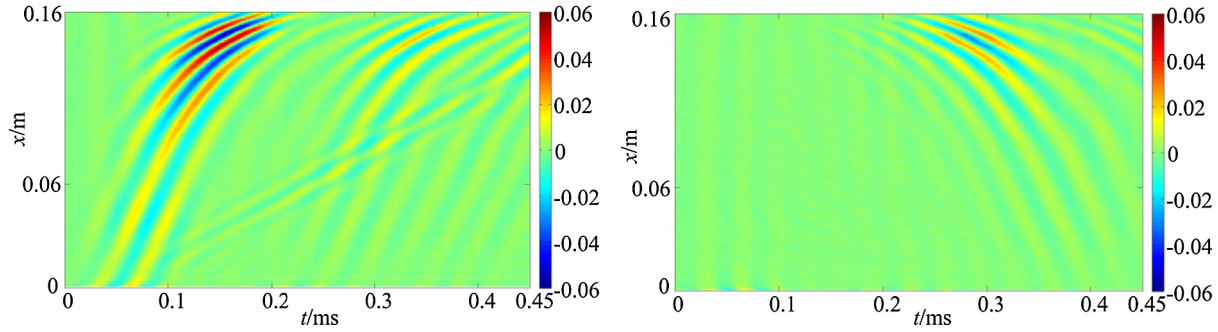

Fig. 15. Wave field: (a) incident signal $v_i(x,t)$; (b) reflected signal $v_r(x,t)$.

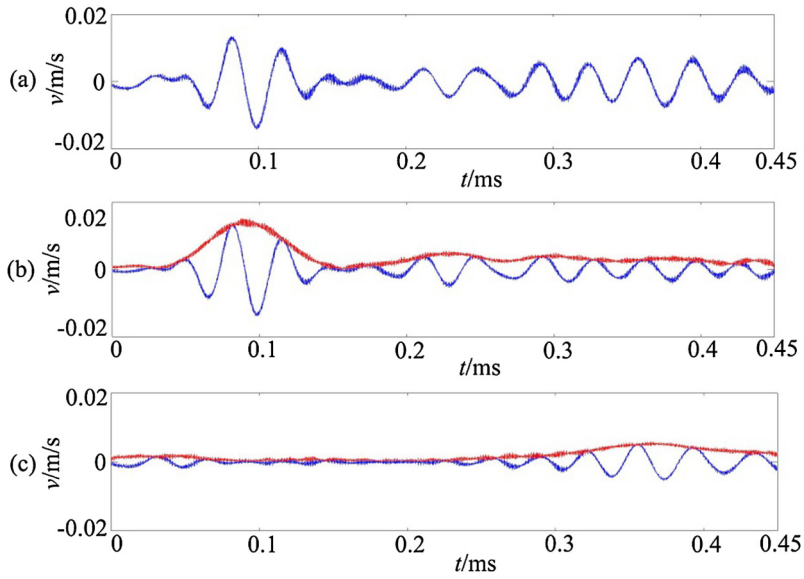

Fig. 16. Signal at $x = 0.06$ m: (a) original wave; (b) incident wave; (c) reflected wave.

at $x = 0.145$ m does not decrease monotonously as the thickness of the damping layer increases. Results also indicate the existence of an optimal thickness of the damping layer to ensure the smallest reflection coefficient although the optimum damping layer thickness is dependent on many factors. Among the five thicknesses tested, the optimal one is around 0.5

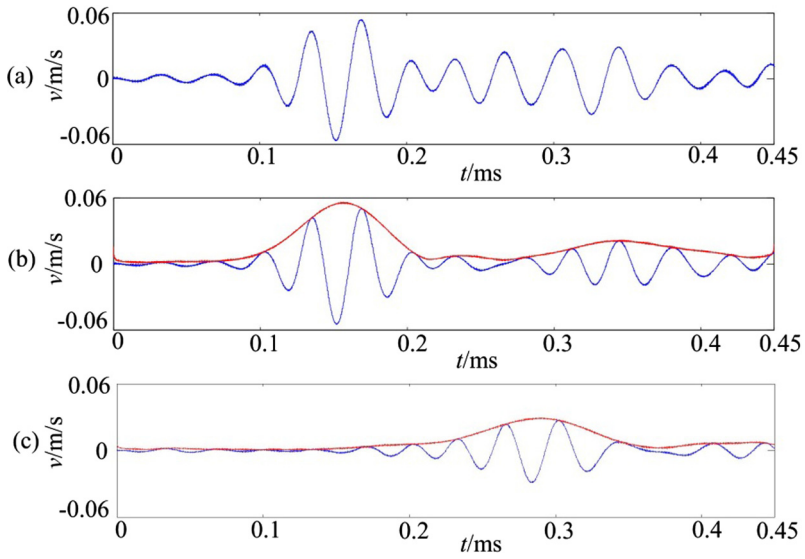

Fig. 17. Signal at $x = 0.145$ m: (a) original wave; (b) incident wave; (c) reflected wave.

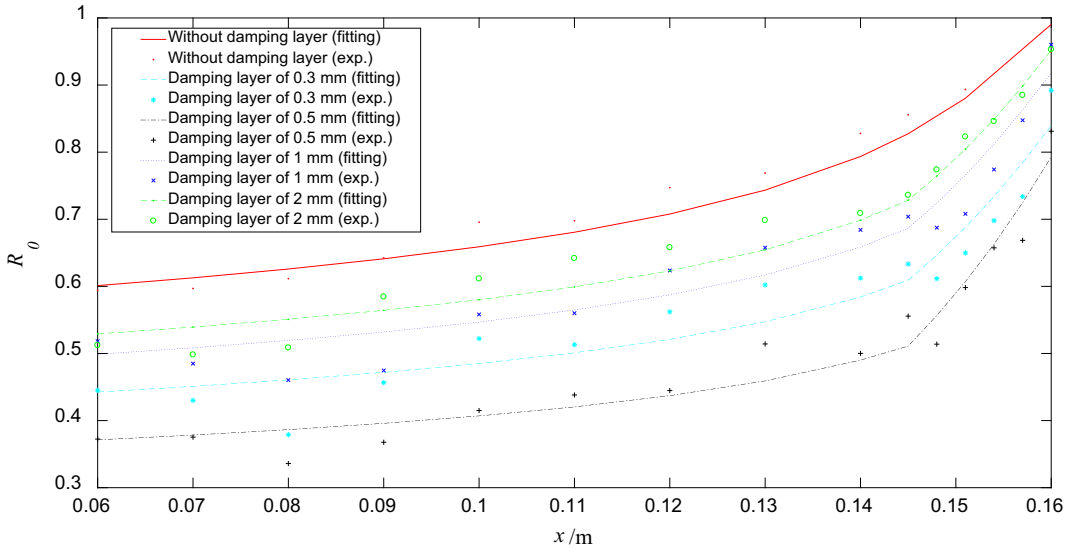

Fig. 18. Reflection coefficient at different location in x direction when damping strips of different thickness are bonded.

mm. Before this optimal value, the reflection coefficient decreases with increasing thickness as a result of the increasing energy dissipation. Exceeding the optimal value, however, the reflection coefficient starts to increase as the damping layer becomes thicker. This indicates an increasing and non-negligible dynamic effect of the damping layer, which starts to adversely compromise the ideal wave propagation pattern of the ABH. Energy dissipation also suffers by the same token.

5. Conclusions

In this paper, a time-domain experimental technique, based on a laser-induced visualization system, is proposed for the investigation of the wave propagation and attenuation in a one-dimensional ABH plate. The proposed method utilizes non-contact excitation and offers a time-domain analysis tool as an alternative to the widely used frequency-domain approaches in order to get a better understanding on various physical phenomena incurred during the wave propagation process through ABH structures.

An analytical expression of the reflection coefficient of flexural waves in a modified one-dimensional ABH is derived and a new procedure is proposed for determining the reflection coefficient based on the wave extraction and separation. Experi-

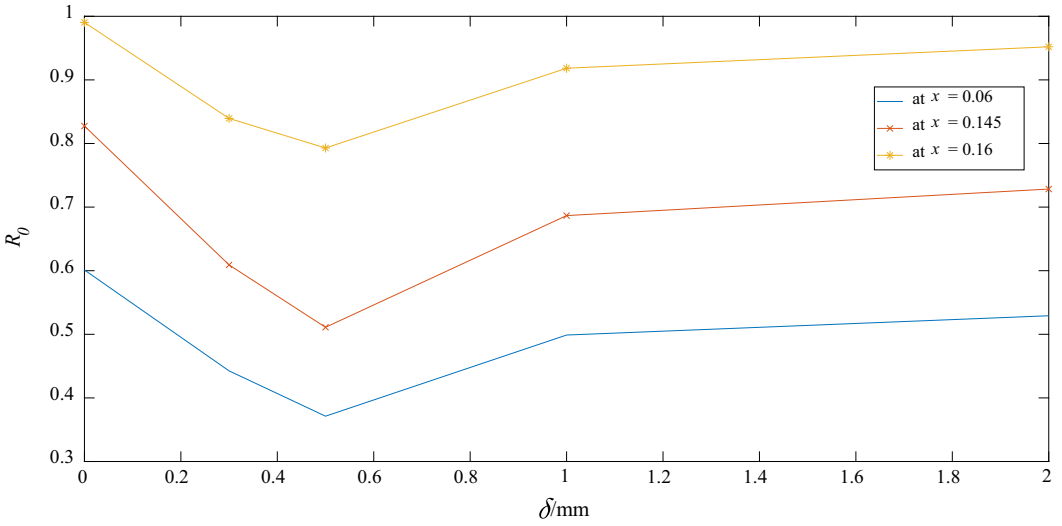

Fig. 19. The influence of the thickness of the damping layer on the reflection coefficient at three different locations.

mental data can be used to calibrate the coefficients used in the analytical expressions of the reflection coefficient. Despite the highly dispersive nature of the waves, reasonably consistent results have been obtained after fitting with a LMS algorithm based on the theoretical expression.

The proposed time-domain method, comprised of a laser-induced visualization technique and the associated signal processing and feature extraction methods, allows for the visualization of the entire wave propagation and reflection process in a non-ideal one-dimensional ABH structure. The validity of the proposed approach is demonstrated by revisiting some of the fundamental issues related to the ABH phenomena, found to be consistent with literature. For example, the phenomena of the wave compression accompanied by the phase velocity decrease and the amplitude increase toward the sharp edge of ABH structure have been clearly demonstrated. The wave velocity obtained from the experimental wave field in the distance-time domain also agrees well with the theoretically predicted velocity variations. It is also experimentally confirmed that there exists an optimal thickness for the damping layer, to strike a balance between the energy focalization due to the ABH effect and the energy dissipation. The excessive use of the damping layer may compromise or even jeopardize the ABH-induced energy focalization due to its dynamic interference with the host structure, leading to a reduced energy dissipation.

The most appealing feature of the proposed technique resides in its ability to reveal and scrutinize the fine physical details (in terms of wave separation and visualization) incurring during the entire wave propagation process. In particular, the location-dependent evolution of the wave reflection coefficient can be obtained and displayed. This allows for assessment and evaluation of the practical design of ABH structures when geometrical or manufacturing imperfections are present.

Acknowledgements

This research was supported by National Natural Science Foundation of China (No. 11532006 & 11372133), Research Grants Council of Hong Kong Special Administrative Region, China (PolyU 152009/15E), Natural Science Foundation of Jiangsu Province, China (No. BK20150061), Aeronautical Science Fund (No. 20161552014), Six talent peaks project in Jiangsu Province (No. JXQC-002) and Research Fund of State Key Laboratory of Mechanics and Control of Mechanical Structures (No. 0515Y02).

References

[1] M.A. Mironov, Propagation of a flexural wave in a plate whose thickness decreases smoothly to zero in a finite interval[J]. Sov Phys. – Acoust. 34 (1988) 318–319.
[2] V.V. Krylov, Localised acoustic modes of a quadratically-shaped solid wedge[J], Moscow Univ. Phys. Bull. 45 (1990) 65–69.
[3] V.V. Krylov, A.L. Shuvalov, Propagation of localized flexural vibrations along plate edges described by a power law[J]. 22(2) (2000) 263–270.
[4] E.P. Bowyer, V.V. Krylov, Experimental investigation of damping flexural vibrations in glass fibre composite plates containing one- and two-dimensional acoustic black holes[J], Comp. Struct. 107 (2014) 406–415.
[5] L. Zhao, S. Conlon, F. Semperlotti, Broadband energy harvesting using acoustic black hole structural tailoring[J], Smart Mater. Struct. 23 (2014) 065021.
[6] L.X. Zhao, Passive vibration control based on embedded acoustic black holes, J. Vibration Acoust. 138 (2016) 041002(6pp).
[7] D.O. Boy, V.V. Krylov, Damping of flexural vibrations in circular plates with tapered central holes[J], J. Sound and Vib. 330 (2011) 2220–2236.
[8] J. Daniel, E.P. Bowyer, V.V. Krylov, Point mobility of a cylindrical plate incorporating a tapered hole of power-law profile[J], J. Acoust. Soc. Am. 129 (2011) 3475–3482.

[9] E.P. Bowyer, V.V. Krylov, Experimental study of sound radiation by plates containing circular indentations of power-law profile[J], App. Acoust. 88 (2015) 30–37.
[10] S.C. Conlon, J.B. Fahnline, F. Semperlotti, Numerical analysis of the vibroacoustic properties of plates with embedded grids of acoustic black holes[J], J. Acoust. Soc. Am. 137 (2015) 447–457.
[11] P.A. Feurtado, S.C. Conlon, An experimental investigation of acoustic black hole dynamics at low, mid and high frequency[J], J. Vib. Acoust. 138 (2016) 61002.
[12] V.V. Krylov, New type of vibration dampers utilizing the effect of acoustic 'black holes'[J], Acta Acustica United Acustica 90 (5) (2004) 830–837.
[13] V.V. Krylov, Acoustic 'black holes' for flexural waves and their potential applications[C], in: Proceedings of the Institute of Acoustics Spring Conference, Salford, UK, 2002, pp. 25–27.
[14] V.V. Krylov, F. Tilman, Acoustic black holes for flexural waves as effective vibration dampers[J], J. Sound Vib. 274 (2004) 605–619.
[15] V.V. Krylov, R.E.T.B. Winward, Experimental investigation of the acoustic black hole effect for flexural waves in tapered plates[J], J. Sound Vib. 300 (1–2) (2007) 43–49.
[16] D.O. Boy, V.V. Krylov, V. Kralovic, Damping of flexural vibrations in rectangular plates using the acoustic black hole effect[J], J. Sound and Vib. 329 (2010) 4672–4688.
[17] V.V. Krylov, Geometrical-acoustics approach to the description of localized vibrational modes of an elastic solid wedge[J], Sov. Phys. Tech. Phys. 35 (2) (1990) 137–140.
[18] V.B. Georgiev, J. Cuenca, F. Gautier, et al, Damping of structural vibrations in beams and elliptical plates using the acoustic black hole effect[J], J. Sound Vib. 330 (11) (2011) 2497–2508.
[19] D. Ross, E.E. Kerwin, E.M. Ungar, Damping of plate flexural vibrations by means of viscoelastic laminae, Structural Damping [B], Pergamon Press, Oxford, 1960, pp. 49–87.
[20] L.L. Tang, S. Zhang, H.L. Ji, et al, Characterization of acoustic black hole effect using a 1-D fully-coupled and wavelet-decomposed semi-analytical model [C], in: INTER-NOISE and NOISE-CON Congress and Conference Proceedings. Institute of Noise Control Engineering, 250(5) (2015) 1619–1630.
[21] J. Moll, T. Wandowski, et al, Experimental analysis and prediction of antisymmetric wave motion in a tapered anisotropic waveguide[J], J. Acoust. Soc. Am. 138 (1) (2015) 299–306.
[22] A. Maurel, J.F. Mercier, S. Felix, Propagation in waveguides with varying cross section and curvature: a new light on the role of supplementary modes in multi-modal methods[C], Proc. R. Soc. London, Ser. A 470 (2014) 20140008.
[23] M.C.E. Kettani, F. Lupp, A. Guillet, Guided waves in a plate with linearly varying thickness: Experimental and numerical results[J], Ultrasonics 42 (2004) 807–812.
[24] E.P. Bowyer, D.J. O'Boy, V.V. Krylov, et al, Effect of geometrical and material imperfections on damping flexural vibrations in plates with attached wedges of power law profile[J], Appl. Acoust. 73 (5) (2012) 514–523.
[25] H. Zhu, F. Semperlotti, Anomalous refraction of acoustic guided waves in solids with geometrically tapered metasurfaces [J], Phys. Rev. Lett. 117 (3) (2016) 034302.
[26] L.X. Zhao, F. Semperlotti, Embedded Acoustic Black Holes for semi-passive broadband vibration attenuation in thin-walled structures [J], J. Sound Vib. 388 (2017) 42–52.
[27] S.L. Yan, A.M. Lomonosov, Z.H. Shen, Evaluation of an acoustic black hole's structural characteristics using laser-generated Lamb waves[J], Laser Phys. Lett. 13 (2016) 025003 (5pp).
[28] W. Huang, H.L. Ji, J.H. Qiu, L. Cheng, Wave energy focalization in a plate with imperfect two-dimensional acoustic black hole indentation[J], J. Vibration Acoust., ASME 138(6) (2016) 061004.1–12.
[29] V. Denis, F. Gautier, A. Pelat, et al, Measurement and modelling of the reflection coefficient of an Acoustic Black Hole termination[J], J. Sound Vib. 349 (2015) 67–79.
[30] C. Zhang, J. Qiu, H. Ji, Laser ultrasonic imaging for impact damage visualization in composite structure[C], in: Proceedings of the 7th European Workshop on Structural Health Monitoring, 2014.
[31] Y. Wu, J. Qiu, C. Zhang, et al, A method to improve the visibility of the damage-reflected wave[J], Chin. J. Lasers 41 (3) (2014) 0308001–308020.
[32] J.R. Lee, C.C. Chia, C.Y. Park, Jeong. Laser ultrasonic anomalous wave propagation imaging method with adjacent wave subtraction algorithm[J], Opt. Laser Technol. 44 (5) (2012) 1507–1515.
[33] C.C. Chia, J.R. Lee, C.Y. Park, H.M. Jeong, Laser ultrasonic anomalous wave propagation imaging method with adjacent wave subtraction: application to actual damages in composite wing[J], Opt. Laser Technol. 44 (2) (2012) 428–440.
[34] T.E. Michaels, J.E. Michaels, M. Ruzzene, Frequency-wavenumber domain analysis of guided wavefields[J], Ultrasonics 51 (51) (2011) 452–466.
[35] M. Ruzzene, Frequency–wavenumber domain filtering for improved damage visualization[J], Smart Mater. Struct. 16 (6) (2007) 2116–2129 (14).
[36] H.F. Zhu, F. Semperlotti, Phononic thin plates with embedded acoustic black holes[J], Phys. Rev. B 91 (104304) (2015) 1–9.
[37] L.L. Tang, L. Cheng, Broadband local resonant bandgaps in periodic structures with embedded acoustic black holes[J], J. Appl. Phys. 121 (2017) (194901).